Understanding how the rate of C–H bond cleavage affects formate oxidation catalysis by a Mo-dependent formate dehydrogenase

William E. Robinson[1,3], Arnau Bassegoda[2], James N. Blaza[2,4], Erwin Reisner[1*], Judy Hirst[2*]

[1] Department of Chemistry, University of Cambridge, Lensfield Road, Cambridge CB2 1EW, U.K.

[2] Medical Research Council Mitochondrial Biology Unit, University of Cambridge, Keith Peters Building, Cambridge Biomedical Campus, Hills Road, Cambridge CB2 0XY, U.K.

[3] Current address: Institute for Molecules and Materials, Radboud University Nijmegen, Heyendaalseweg 135, 6525 AJ Nijmegen, The Netherlands

[4] Current address: Department of Chemistry, University of York, Heslington, York YO10 5DD, UK.

* reisner@ch.cam.ac.uk, jh@mrc-mbu.cam.ac.uk

Abstract

Metal-dependent formate dehydrogenases (FDHs) catalyze the reversible conversion of formate into CO_2, a proton and two electrons. Kinetic studies of FDHs provide key insights into their mechanism of catalysis, relevant as a guide for the development of efficient electrocatalysts for formate oxidation as well as for CO_2 capture and utilization. Here, we identify and explain the kinetic isotope effect (KIE) observed for the oxidation of formate and deuterioformate by the Mo-containing FDH from *Escherichia coli* using three different techniques: steady-state solution kinetic assays, protein film electrochemistry (PFE) and pre-steady state stopped-flow methods. For each technique, the Mo center of FDH is reoxidized at a different rate following formate oxidation, significantly affecting the observed kinetic behavior and providing three different viewpoints on the KIE. Steady-state turnover in solution, using an artificial electron acceptor, is kinetically limited by diffusional intermolecular electron transfer, masking the KIE. In contrast, interfacial electron transfer in PFE is fast, lifting electron transfer rate limitation and manifesting a KIE of 2.44. Pre-steady state analyses using stopped-flow spectroscopy revealed a KIE of 3 that can be assigned to the C–H bond cleavage step during formate oxidation. We formalize our understanding of FDH catalysis by fitting all the data to a single kinetic model, recreating the condition-dependent shift in rate-limitation of FDH catalysis between active site chemical catalysis and regenerative electron transfer. Furthermore, our model predicts the steady-state and time-dependent concentrations of catalytic intermediates, providing a valuable framework for the design of future mechanistic experiments.

Introduction

Metal-dependent formate dehydrogenases (FDHs) are paradigm electrocatalysts for the interconversion of CO_2 and formate,[1,2] and play a versatile range of roles in biological systems.[3] The FDHs from several organisms, including *Desulfovibrio desulfuricans,*[4] *Rhodobacter capsulatus,*[5] *Cupriavidus necator* (formerly *Ralstonia eutropha*),[6] *Escherichia coli,*[2] *Syntrophobacter fumaroxidans,*[1,7] *Acetobacterium woodi*,[8] *Methylobacterium extorquens,*[9] *Rhodobacter aestuarii*[10] and *Methanococcus maripaludis,*[11] have all been reported to catalyze both formate oxidation and CO_2 reduction in assays using solution electron donors/acceptors, although their relative rates of CO_2 reduction vary widely. The enzymes from *S. fumaroxidans*, *D. vulgaris* Hildenborough and *E. coli*, which are the W-dependent FDHs *Sf*FDH1[1] and *Dv*FDH[12,13] and the Mo-dependent *Ec*FDH-H,[2] have further been shown to perform thermodynamically-reversible (efficient) reduction of CO_2 to formate when immobilized on electrodes. In this case, the driving force for electron transfer to and from the enzyme active site to support catalysis is controlled by the electrode potential, and much greater rates of turnover can be achieved than in solution, particularly for CO_2 reduction. Recently, the high activity of FDHs has motivated their incorporation into colloidal and electrochemical devices capable of efficient light-driven CO_2 reduction,[12–16] into enzymatic formate fuel cells,[17] and semi-artificial mimics of formate hydrogenlyase systems.[18] These systems often function with high thermodynamic efficiency, enabled by FDH electrocatalysis.

Although FDHs provide an excellent opportunity to define an efficient mechanism for CO_2 activation and reduction, as well as for the reverse formate oxidation reaction, their mechanisms remain only poorly understood.[19] Several X-ray crystal structures of the oxidized states of Mo/W-containing FDHs have been described.[20–24] All show the active site (Figure 1), consisting of a central Mo or W ion coordinated by two pterin (dithiolene) cofactors, adjacent to an iron-sulfur cluster that collects or delivers electrons (*via* single-electron transfer) to couple catalysis at the Mo/W site to a partner reaction (for example, NAD^+/NADH interconversion or quinone reduction) at a separate site. The Mo/W is also coordinated by a terminal sulfido group[22,25,26] and a selenocysteine (Sec)[27] or cysteine (Cys)[5] residue. Conserved arginine (Arg) and histidine (His) residues are present in the outer coordination sphere. The roles of the Sec (or Cys), His and Arg residues in catalysis have not yet been confirmed, but they are probably involved in proton transfer and/or stabilizing substrates and intermediates. A central question in FDH catalysis is whether the Sec remains coordinated to the metal center throughout catalysis,[6] or whether it dissociates to provide a vacant site for substrate binding.[28] Although the reduced form of FDH-H from *E. coli* lacks definitive structural characterization because there are two conflicting interpretations of the only available crystallographic data[21], evidence from iodoacetamide tagging[26,29] and inhibitor-binding experiments[28,30] has suggested that formate displaces Sec (or Cys) from the metal center. In contrast, this suggestion has recently been challenged by the crystal structure of FDH-AB from *D. vulgaris* Hildenborough, in which the active site Sec is clearly coordinated to the W center in the reduced W(IV) state – albeit in the absence of any substrate or product in the active site.[24]

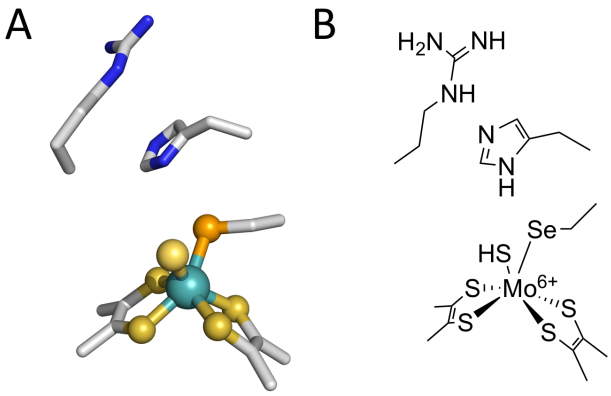

Figure 1. The active site of metal-dependent formate dehydrogenases. **A**: The X-ray crystal structure of the oxidized active site of *Ec*FDH-N (PDB number: 1KQF).[20] **B**: Schematic reproduction of (A).

Molybdoenzymes typically cycle between the Mo(VI), Mo(V) and Mo(IV) states.[31] Recently, a reduction potential of −0.265 V *vs*. the standard hydrogen electrode (SHE) has been measured electrochemically and assigned to the Mo center of a truncated FDH from *C. necator*, though it is unclear whether this potential corresponds to the Mo(VI/V) or Mo(V/IV) couple.[32] Electron paramagnetic resonance (EPR) spectra of formate or dithionite reduced FDHs exhibit a characteristic Mo(V) signal.[33–35] Following the two electron reduction of the Mo(VI) state by formate [Mo(VI) + $HCOO^-$ → Mo(IV) + H^+ + CO_2] the Mo(IV) state is oxidized by a nearby cofactor, generating

the Mo(V) state. In FDHs such as *Ec*FDH-H that contain only one iron-sulfur center, the Mo(V) state is stable in the absence of an external electron acceptor. EPR spectra have revealed strong magnetic coupling between the Mo(V) center and a solvent-exchangeable proton[33–35] that has been attributed to a Mo(V)–SH group, formed by a formal hydride transfer from formate to the Mo(VI)=S group, followed by one-electron oxidation of the resulting Mo(IV)–SH state.[27,34,35] The mechanism by which this formal hydride transfer occurs, either by concerted hydride transfer[6] or proton-coupled electron transfer (PCET),[28] remains under debate. Therefore, gaining a deeper understanding of the kinetics and intermediates present during FDH catalysis is crucial for developing a full picture of the CO_2/formate interconversion mechanism.

Here, we have investigated the kinetic isotope effect (KIE) for formate ($HCOO^-$ and $DCOO^-$) oxidation by *Ec*FDH-H (referred to hereon as FDH) using three distinct kinetic methods: classical steady-state solution assays with an additional soluble electron acceptor, steady-state electrocatalysis with electrode-immobilized FDH and the electrode as electron acceptor, and single-turnover stopped-flow spectroscopy in which formation of the Mo(V) state is monitored in the absence of an external electron acceptor. The three methods provide different perspectives on the KIE and its relevance in determining the rate of catalysis. They allow us to explore two regimes of rate limitation, one in which formate oxidation catalysis is limited by electron transfer (solution assays), the other in which chemical catalysis is more dominant (electrocatalysis and stopped flow experiments). We propose a unifying kinetic model that allows the three data sets to be reconciled, despite their qualitative differences. When fitted to the data, our model provides a conceptual framework for the rationalization of FDH catalysis in terms of both the rate of active site catalysis and the rate of electron transfer to terminal electron acceptors. As a result, it allows prediction of the steady-state and time-dependent concentrations of key FDH states, allowing us to hypothesize the conditions under which key intermediates in CO_2/formate interconversion may be observed during steady state turnover, and the timescales of their transient lifetimes.

Understanding how the catalysis of reversible and efficient formate oxidation is achieved is directly relevant to the catalysis of reversible and efficient CO_2 reduction. Both reactions require the challenging feat of efficient, simultaneous formation/breakage of C–H and C=O bonds. Developing knowledge of them may be exploited in the design of advanced electrocatalysts for CO_2 reduction, just as hydrogenases have inspired the field of hydrogen evolution catalysis.[36,37] FDH provides a template for both the inner and outer spheres of future bidirectional and reversible synthetic electrocatalysts.[38–40] Furthermore, understanding the fundamental behavior of FDHs will inform the development of future (photo)electrochemical devices, aiding the selection of appropriate electron donors/acceptors and optimal operating conditions.

Experimental Section

Materials: *Ec*FDH-H was isolated and purified as reported previously.[2] 2-(N-morpholino)ethanesulfonic acid (MES, Alfa Aesar), N-tris(hydroxymethyl)methyl-3-aminopropanesulfonic acid (TAPS, Sigma Aldrich), 4-(2-hydroxyethyl)-1-piperazineethanesulfonic acid (HEPES, Sigma Aldrich), potassium acetate (Alfa Aesar), sodium hydrogen carbonate (Breckland Scientific), sodium carbonate (Breckland Scientific), sodium azide (Fisher), sodium nitrate (Sigma Aldrich), benzyl viologen (Sigma Aldrich) and disodium hydrogen phosphate (Sigma Aldrich) were purchased at the highest available quality and used as received. Sodium formate (Sigma Aldrich) and sodium deuterioformate (Sigma Aldrich, 99 atom%) were dried at 100 °C under vacuum before use to ensure accurate weight measurement. Buffer solutions were prepared using MilliQ water (18 MΩ cm, 25 °C) and their pH values corrected using concentrated NaOH, KOH or H_2SO_4.

Solution assays: Rates of formate oxidation by *Ec*FDH-H were monitored by measuring the coupled reduction of benzyl viologen (BV^{2+}) in solutions containing varying amounts of sodium formate, 1 mM BV^{2+} and 50 mM phosphate buffer (pH 7.5, 25 °C). The increasing absorbance of BV^+ (ε_{578} = 8.65 mM^{-1} cm^{-1}) was monitored following addition of *Ec*FDH–H in 200 µL wells in a Molecular Devices microtiter plate reader housed in an anaerobic N_2-filled glovebox.

Protein film electrochemistry (PFE): PFE was performed using an Ivium Compactstat potentiostat in a N_2-filled glovebox (<1 ppm O_2). A three-electrode cell, held at 23.5 °C using a circulated water jacket, was used to house a Pt mesh counter electrode, an Ag/AgCl/saturated KCl reference electrode and a graphite-epoxy composite rotating disk electrode (RDE, area 0.09 cm^2, fabricated as described previously[2]) with a rotation rate of 2,000 rpm.[28] Experiments were performed in pH-buffered solutions containing 25 mM of each of MES, TAPS, HEPES and K^+acetate.

*Ec*FDH-H films were prepared as reported previously.[28] Sodium (deuterio)formate solutions were prepared at the same pH and buffer concentration as the cell solution. Chronoamperometric measurements of *Ec*FDH-H formate oxidation kinetics were performed by holding the electrode potential at 0 V *vs*. SHE and continually titrating the solutions of sodium (deuterio)formate into the electrochemical cell whilst the current was monitored. Prior to measuring the rate of formate oxidation, the electrode potential was poised at –0.6 V *vs*. SHE for 10 s to allow for reductive activation of FDH.[28] As reported previously, high-frequency noise from the RDE motor was removed using Fourier transformation (Figure S1A).[28] Then, the degradation of the enzyme film was described by taking linear fits of each step of the titration. The chronoamperometric data were divided by the resulting decay function (Figure S1B) to remove the effect of film degradation (Figure S1C).[41]

Stopped-flow experiments: The reduction of oxidized *Ec*FDH-H by formate was measured using a stopped-flow apparatus connected to a photodiode array spectrometer (Applied Photophysics Ltd.) housed in an anaerobic N_2 filled glovebox at 25 °C . Solutions of enzyme containing variable amounts of sodium azide were made up in 100 mM MES buffer at pH 6 (to improve the FDH stability) and then mixed in a 1:1 (v:v) ratio with a solution of 20 mM formate (also in 100 mM MES buffer at pH 6). Spectra were recorded from 300 to 723 nm with a step of 2 nm and the sum of the absorbances at 436 to 444 nm were analyzed as first-order decay curves. Spectra recorded before and after reduction of FDH with formate are shown in Figure S2.

Results and Discussion

Methods to study the KIE of FDH catalysis

The solution kinetic assay, protein film electrochemistry (PFE) and stopped-flow methodologies used to study formate oxidation by FDH are summarized in Figure 2.

The solution assays (Figure 2A) employ benzyl viologen ($BV^{2+} \rightarrow BV^{+}$) as electron acceptor to enable homogeneous formate oxidation with two molecules of BV^{2+} being required to oxidize one formate molecule. Electrons are transferred sequentially, one-by-one, from the Mo-containing active site to two molecules of BV^{2+} via the $[Fe_4S_4]$ center. This diffusional and tetramolecular steady-state process has previously been described using reciprocal-plot analyses to determine basic kinetic parameters for FDH catalysis.[42] Measuring the initial rate of BV^{2+} reduction defines the steady-state rate of formate oxidation.

In contrast, PFE (Figure 2B) uses an electrode to drive heterogeneous formate oxidation. FDH, immobilized on an electrode surface, is immersed in a solution of formate in a standard 3-electrode cell. The electrode is rotated to supply formate and disperse the CO_2 product. Electronic communication between the electrode and the immobilized FDH units allows catalysis to be controlled by the electrode potential.[43] As interfacial electron transfer can be driven much faster than the diffusion-limited electron transfer required in solution assays, PFE offers an improved opportunity to focus attention on the fast enzyme-catalyzed reaction kinetics.

Finally, stopped-flow spectroscopy was used to monitor the single-turnover reduction of the $[4Fe\text{-}4S]^{2+}$ cluster of FDH upon mixing it with formate (in the absence of a terminal electron acceptor). The only electron transfer step, following substrate oxidation, is the single electron transfer from the Mo to the $[4Fe\text{-}4S]^{2+}$ cluster (Figure 2C), which is reduced stoichiometrically due to its higher reduction potential. Therefore, stopped-flow kinetic data report only on reaction kinetics intrinsic to FDH.

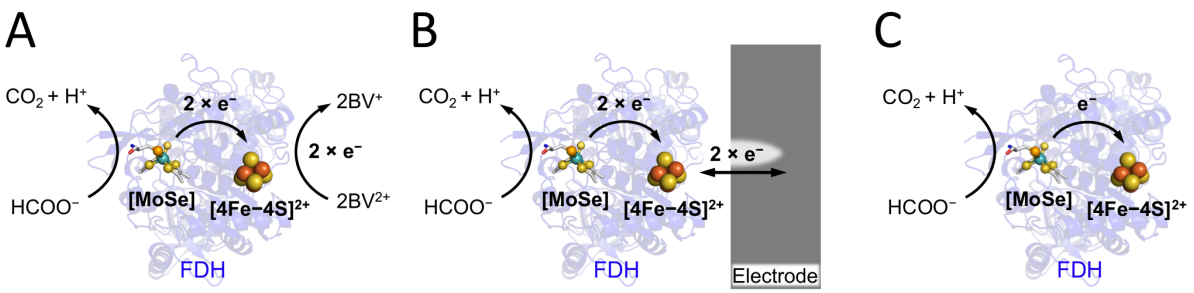

Figure 2. Summary of the methods used to study formate oxidation by *Ec*FDH–H. Formate is oxidized at the FDH Mo-containing active site; the active site transfers two electrons (one at once) to the $[4Fe–4S]^{2+}$ cluster, which in turn transfers them to the external electron acceptor. **A:** In solution assays, benzyl viologen (BV^{2+}) accepts the electrons from steady-state formate oxidation. **B:** In PFE an electrode accepts the electrons reversibly from steady-state formate oxidation. **C:** In stopped-flow spectrometry a single formate molecule is oxidized by the Mo(VI) active site then one electron is transferred to the $[4Fe–4S]^{2+}$ cluster.

Steady-state formate oxidation in solution

Figure 3 shows the rate of formate oxidation (as a function of the $HCOO^-$ or $DCOO^-$ concentration) measured in solution kinetic assays with 1 mM BV^{2+}.[2,42] Both data sets are consistent with Michaelis-Menten kinetics, except that the rate decreases at high $HCOO^-$ concentrations (Figure 3, circled points). We are currently unable to provide a clear rationale for this observation: it is suggestive of inhibition from the binding of $HCOO^-$ to reduced FDH states, but a similar effect would then be expected for $DCOO^-$ and is not observed. Although the unexplained downward trend obscures definitive measurements at high concentration, the best fit to the data (discounting these points) suggests that there is no KIE in the substrate-independent rate of formate oxidation, V_{max} (V_{max}^H = 60.1 ± 1.6 $mol_{formate}$ s^{-1} mol_{FDH}^{-1}, V_{max}^D= 59.65 ± 0.95 $mol_{formate}$ s^{-1} mol_{FDH}^{-1}, V_{max}^H/V_{max}^D = 1.01 ± 0.03). This result implies that the rate limiting step at high concentration is not C–H/D bond cleavage, or any reaction coupled strongly to it. Strikingly, however, a clear KIE is evident at low formate concentrations, where increasing the $HCOO^-$ concentration has a much stronger effect than increasing the $DCOO^-$ concentration. This difference is reflected by K_M^D being higher than K_M^H (K_M^D = 158 ± 8 μM and K_M^H = 58 ± 8 μM) and by the second order rate constant for $DCOO^-$ being lower than for $HCOO^-$ (k_2^D = 0.37 ± 0.02 s^{-1} μmol_{FDH}^{-1} and k_2^H = 1.0 ± 0.1 s^{-1} μmol_{FDH}^{-1}, k_2^H/k_2^D = 2.77 ± 0.41). The results suggest that:

i) $HCOO^-$ binds more tightly or rapidly to the active site than $DCOO^-$, and/or
ii) at low formate concentrations, the rate limiting step is both isotope and concentration sensitive (at high concentrations the rate of this step increases sufficiently that it overtakes a new rate limiting step, such as electron transfer to BV^{2+}).

A difference in binding between $HCOO^-$ and $DCOO^-$ [hypothesis (i)] is hard to rationalize for only a simple formate binding step (without any degree of C–H bond cleavage), which must be essentially isotope independent. However, an initial binding step that is both concentration and isotope dependent may be rationalized either by strong kinetic coupling between the binding and C–H bond cleavage processes (a short lived Michaelis complex that reacts as soon as it is formed) or by partial proton (or hydride) transfer upon binding, replacing the simple Michaelis complex by a 'charge-transfer' intermediate such as the five-membered ring intermediate proposed previously.[28]

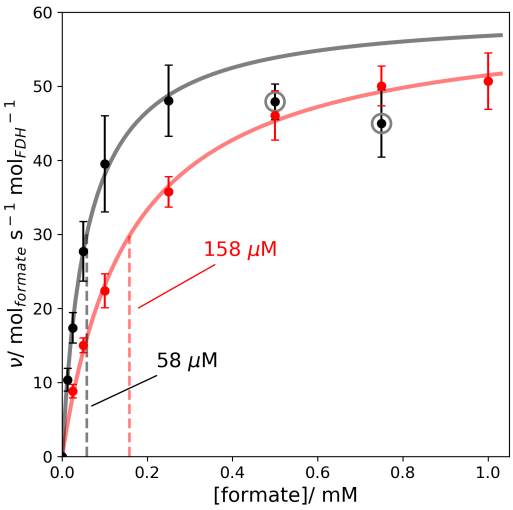

Figure 3. Rates of $HCOO^-$ (black dots) and $DCOO^-$ (red dots) oxidation determined by solution assays. Conditions: 1 mM BV^{2+}, 25 °C, pH 7.5, 25 mm MES, TAPS, HEPES, K^+ acetate. Error bars are ± standard error from triplicate experiments. The lines were calculated according to the Michealis-Menten equation (rate = $V_{max}[HCOO^-]/\{K_M + [HCOO^-]\}$) with K_M^H = 58 μM, V_{max}^H = 60.10 $mol_{formate}$ s^{-1} mol_{FDH}^{-1} (black), by neglecting the two highest concentration formate points (circled), K_M^D = 158 μM, V_{max}^D = 59.65 $mol_{formate}$ s^{-1} mol_{FDH}^{-1} (red).

Electrocatalytic formate oxidation

Figure 4A compares previously published PFE data on the rate of $HCOO^-$ oxidation[28] with new data for $DCOO^-$ oxidation. Both data sets exhibit Michaelis-Menten profiles with no decrease in rate at high $HCOO^-$ concentration. Although the unknown electroactive surface coverage of FDH on the electrode prevents the determination of turnover numbers, the ratio V_{max}^H/V_{max}^D was determined using a chronoamperometic method to directly compare the relative currents, and so account for irreproducibility and instability in the FDH film (Figure 4B). Specifically, catalytic currents were monitored whilst a solution consisting of $HCOO^-$ was diluted stepwise by the addition of $DCOO^-$ (and *vice-versa*) (Figure S3). The two datasets shared identical compositions of $DCOO^-/HCOO^-$, aside from the two extreme points, allowing the rate in $DCOO^-$ to be matched to that in $HCOO^-$. The ratio $V_{max}^H/V_{max}^D = 2.44 \pm 0.05$ is substantially larger than the value determined in solution assays, showing that the rate limiting step at high concentration is isotope dependent and involves C–H bond cleavage. As in the solution assays, there is also an isotope effect on K_M (K_M^H = 0.79 ± 0.03 mM and K_M^D = 0.4 ± 0.1 mM) and on the second order rate constant (k_2^H/k_2^D = 1.2 ± 0.3). The KIE observed for k_2 is consistent with that observed in the solution assays, although smaller (1.2 and 2.77, respectively). However, the effects on K_M are in the opposite direction: in the PFE experiments, K_M^D is lower than K_M^H. Although this result seems counter-intuitive and suggestive of an inverse isotope effect, it arises only from the much lower V_{max} value with $DCOO^-$, which truncates the curve before the full substrate concentration dependence is exhibited.

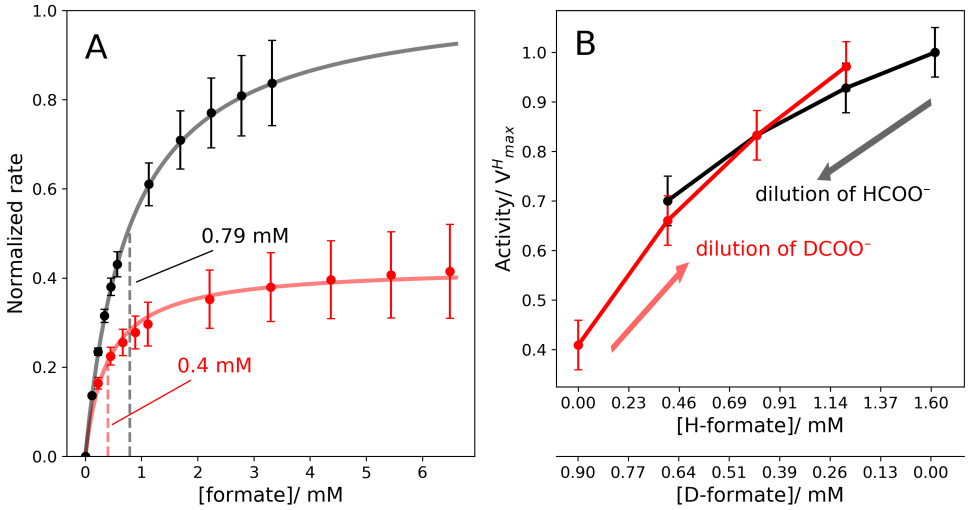

Figure 4. **A:** Rates of $HCOO^-$ (black) and $DCOO^-$ (red) oxidation in PFE experiments (normalized so that $V_{max}{}^H = 1$ and $V_{max}{}^d = 0.41$). Dots: data, lines: fit to the Michealis-Menten equation ($v = V_{max}[H/DCOO^-]/\{K_M + [H/DCOO^-]\}$) with $K_M{}^H = 0.79$ mM, $K_M{}^D = 0.4$ mM. Conditions: 0 V vs SHE, 23.5 °C, pH 7, 25 mM MES, TAPS, HEPES, K^+ acetate. The $HCOO^-$ oxidation PFE data have been presented previously.[28] The error bars show the standard error of the mean. **B:** Determination of the KIE on V_{max} via PFE: Black dots: normalized currents in an experiment in which $HCOO^-$ (concentration steps: 1.6, 1.2, 0.8, 0.4 mM) was diluted with $DCOO^-$ (concentration steps: 0, 0.22, 0.44, 0.66 mM) red dots: normalized currents in an experiment in which $DCOO^-$ (concentration steps: 0.88, 0.66, 0.44, 0.22 mM) was diluted with $HCOO^-$ (concentration steps: 0, 0.4, 0.8, 1.2 mM); the normalization constants were adjusted to overlay to the two datasets. Error bars denote estimated error values derived from several measurements in similar solution compositions.

Single-turnover stopped-flow kinetics

Stopped-flow experiments were used to follow $[4Fe–4S]^{2+}$ reduction as a proxy (assuming intramolecular electron transfer is fast) for the reaction of the Mo(VI) center in FDH with $HCOO^-$ or $DCOO^-$. Experiments were performed at pH 6 using 10 mM formate at several concentrations of N_3^-, a known reversible inhibitor of formate oxidation (Figure 5A, Figure S4). Inhibition was required as the rate of formate oxidation was otherwise too fast to monitor.[28,34,42] A similar stopped-flow study on *C. necator* FDH adopted a different strategy to overcome this challenge, by carrying out experiments at 10 °C to slow the reaction down.[35] Here, we have favored azide inhibition as a strategy to slow FDH catalysis, as we have characterized its inhibition mechanism previously.[28] The spectroscopic traces exhibited mono-exponential behavior and pseudo-first order rate constants determined from the spectroscopic time traces were proportional to $1/[N_3^-]$ (Figure 5B), consistent with the reversible inhibition[34] of formate oxidation by N_3^- described previously,[28] and with fast N_3^- binding/dissociation pre-equilibria. Comparison of the pseudo-first-order rate constants revealed a KIE of 3.2 ± 0.3 (obtained by taking k_H/k_D at equivalent $[N_3^-]$). The isotope-dependence of the formate oxidation rate implies that cleavage of the formate C–H bond is a key rate-limiting process. The KIE determined in this work is of similar magnitude to that previously reported for *C. necator* FDH of 2.1.[35]

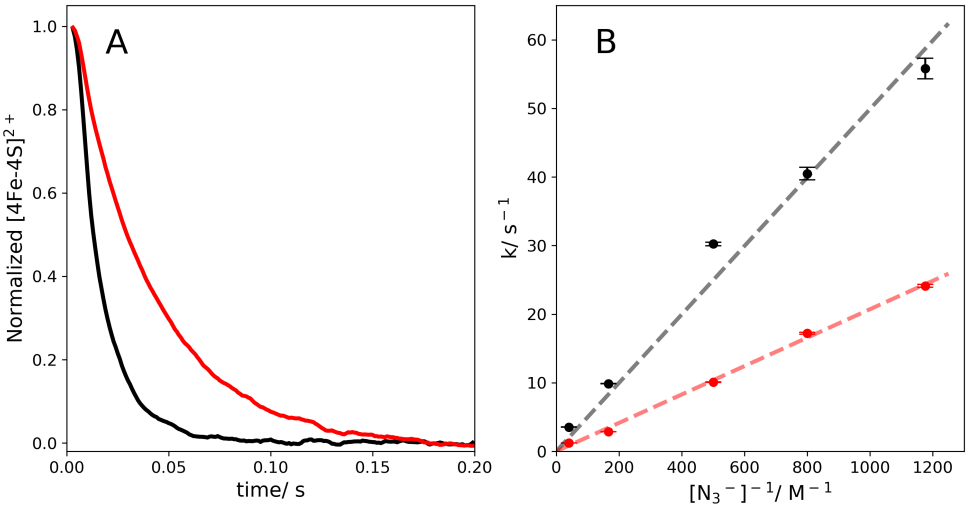

Figure 5. A: Example stopped-flow data reporting on the rate of reduction of the $[4Fe\text{-}4S]^{2+}$ cluster (from the average decay in absorbance, A, from 436 to 444 nm) upon reaction of *Ec*FDH-H with $HCOO^-$ (black trace) and $DCOO^-$ (red trace) in the presence of 0.85 mM N_3^-. Normalisation applied = $(A–A_\infty)/(A_0–A_\infty)$ and data were smoothed to remove noise. **B:** Plots of $1/[N_3^-]$ vs k (rate constant for reduction of the $[4Fe–4S]^{2+}$ cluster) determined from stopped-flow data. Dots: experimental values from the data in panel A and Figure S4; lines: linear fits to data; error bars: the standard error of the fit. Red: $DCOO^-$, Black: $HCOO^-$. Conditions: pH 6, 10 mM formate, 100 mM MES, 25 °C.

Development of a kinetic scheme to describe the data

The data from all three techniques may be explained using the single, unifying model shown in Scheme 1 (see Supplementary Information Section 2 and Figure S5 for details and assumptions on the construction of Scheme 1). In Scheme 1, formate binds to the Mo(VI)=S state and formally transfers a hydride to generate the Mo(IV)–SH(CO_2) state.[35] CO_2 was not added to experimental solutions and therefore dissociates irreversibly to produce the Mo(IV)–SH state, which is then oxidized by one electron to form the stable Mo(V)–SH intermediate. The stopped-flow experiment explores stoichiometric formate oxidation and terminates here (with an irreversible intramolecular k_{ox} step that combines with the preceding irreversible CO_2 dissociation to form k_3),[33–35] whereas in solution assays and PFE a PCET step regenerates the oxidized Mo(VI)=S state to sustain the catalytic cycle. In the latter two cases, electron transfer between the active site and the outside is considered as a single step, without taking into account intramolecular transfer to the $[4Fe–4S]^{2+}$ cluster, which is considered fast (estimated[44] as 4 x 10^6 s^{-1}, much faster than turnover, from the short ~7 Å distance[21,45] and a ΔE of –0.3 V, in excess of the ΔE estimated for the truncated FDH from *C. necator*[32]).

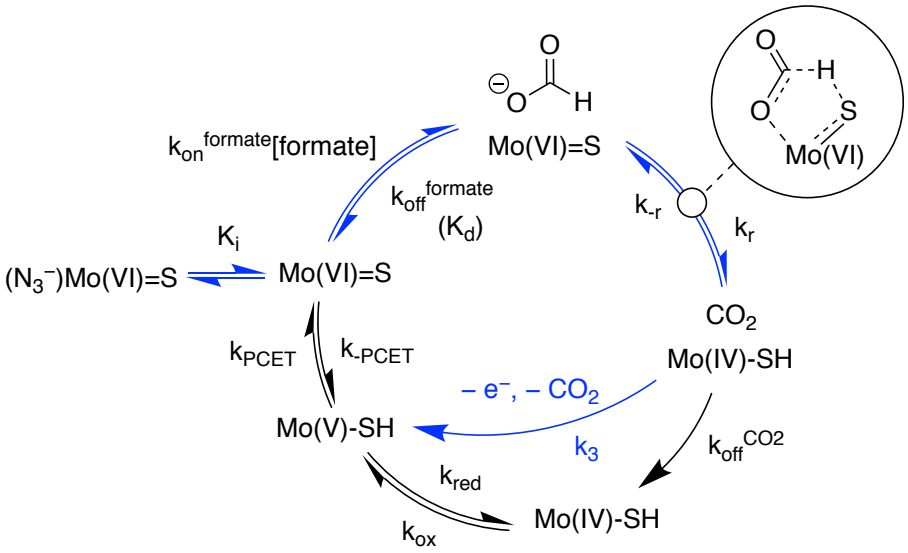

Scheme 1. Catalytic cycle used to model data on formate oxidation from solution assays, PFE and stopped-flow experiments. Blue arrows represent the sub-scheme used to describe the stopped-flow data, ending at the Mo(V)–SH state. A proposed intermediate[28] is shown circled (top right).

The steady-state Equation 1, was derived from Scheme 1 (along with similar equations to describe the population of each species, see Supplementary Information Section 3, equations S1 to S20) by assuming formate binding is fast such that the ratio of Mo(VI)=S and Mo(VI)=S(formate) is set by the equilibrium constant, K_d.

$$v = \frac{k_{off}^{CO_2}\Gamma}{\left[\frac{k_{-r}+k_{off}^{CO_2}}{k_r}.\frac{K_d+[F]}{[F]}+\left(\frac{k_{-PCET}}{k_{PCET}}\frac{K_d}{[F]}\frac{k_{-r}+k_{off}^{CO_2}}{k_r}+\frac{k_{off}^{CO_2}}{k_{PCET}}\right)\left(1+\frac{k_{red}}{k_{ox}}\right)+\frac{k_{off}^{CO_2}}{k_{ox}}+1\right]}$$

Equation 1. Steady-state equation for FDH catalysis derived from Scheme 1. The symbol [F] denotes formate concentration and Γ denotes either the electroactive surface coverage or the solution concentration of FDH.

Equation 2 describes how the population of the Mo(V)–SH state changes over time in stopped-flow experiments. It was derived, along with equations describing the time-dependent evolution of each species (see Supplementary Information Section 4, equations S21 to 48) by assuming both N_3^- and formate binding are fast and can be considered as pre-equilibria.

$$[Mo(V)-SH](t) = [Mo(VI)]_0\left[1-\frac{\beta}{\beta-\gamma}e^{-\gamma t}+\frac{\gamma}{\beta-\gamma}e^{-\beta t}\right]$$

Equation 2. Pre-steady state equation for Scheme 1 in which the reaction terminates at Mo(V)–SH. Definitions: $\beta = \frac{1}{2}\left(k_{-r}+k_3+\frac{k_r}{A}\right)+\frac{1}{2}\sqrt{\left(k_{-r}+k_3+\frac{k_r}{A}\right)^2-\frac{4k_rk_3}{A}}$, $\gamma = \frac{k_rk_3}{A\beta}$, $A = \frac{K_d}{[F]}\left(1+\frac{[N_3^-]}{K_i}\right)+1$, $[Mo(VI)]_0$ = initial concentration (t = 0) of [Mo(VI)] (= [Mo(VI)=S] + [Mo(VI)=S(HCOO⁻)] + [Mo(VI)=S(N_3^-)]).

Finally, as the isotope-sensitive step is expected to be the C–H bond cleavage step, KIE was assigned as a divisor of k_r and k_{-r} in calculations of $DCOO^-$ oxidation rates in Equations 1 and 2.

Modelling the data

Equations 1 and 2 were used to model the data in Figures 3, 4, and 5. An additional PFE data set reporting on $HCOO^-$ oxidation as a function of its concentration at pH 6 (Figure 6D)[28] was included to aid incorporation of the stopped-flow data, which was obtained at pH 6 (lower than the solution and PFE data for experimental and enzyme stability reasons). Table S1 summarizes the rate constants relevant to each data set, and the boundaries

placed on the parameter space searched. Only the K_d values (which were allowed to vary with the pH) and the interfacial/intramolecular electron transfer rate constants were allowed to vary between the datasets.

The parameter space was searched for combinations of parameters which best replicated the data using an evolutionary algorithm (see Supplementary Information Section 5). Many different combinations that could reproduce the data equally well were identified, precluding definition of individual parameter values. However, all parameter combinations that fit the data defined similar steady-state populations and time courses for the different species that comprise Scheme 1, providing new insights into FDH catalysis.

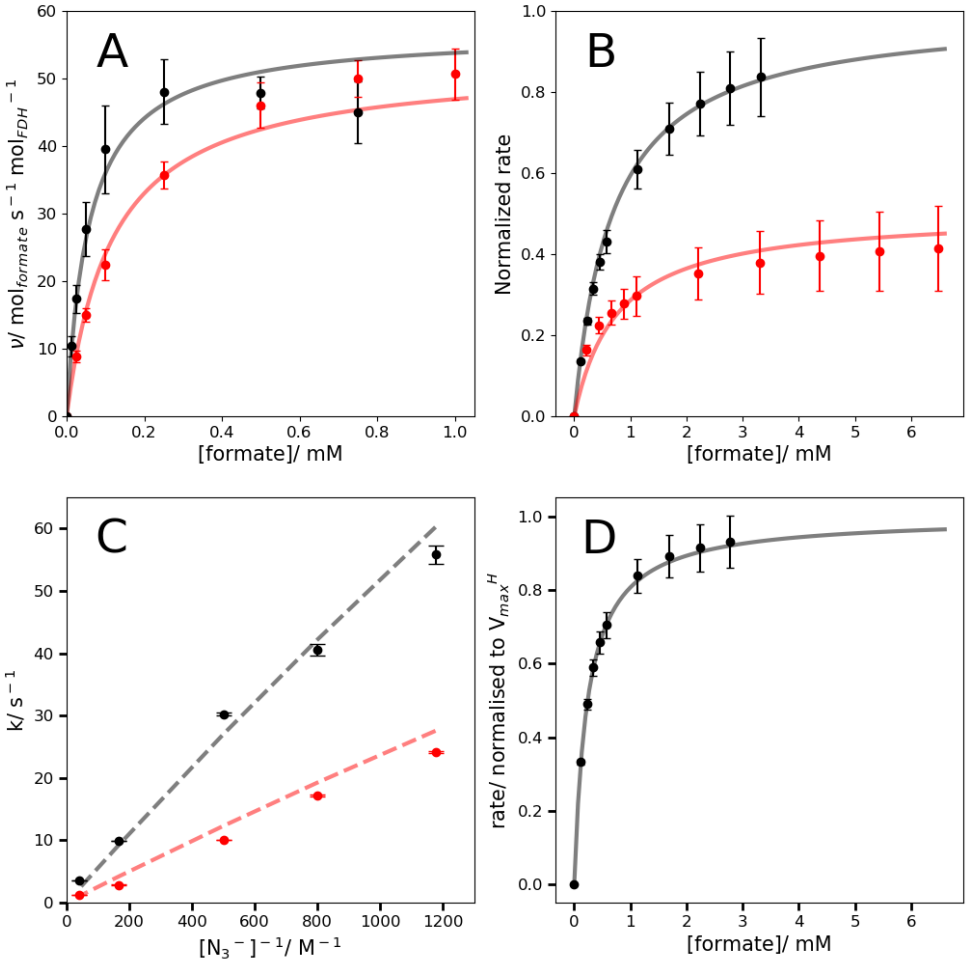

Figure 6. An example of fitting the data by using Scheme 1. **A:** Solution kinetic assays of the rate of formate oxidation at pH 7.5 (black: $HCOO^-$, red: $DCOO^-$, dots: data from Figure 3, line: fit), **B:** PFE measurement of the rate of formate oxidation at pH 7 (black: $HCOO^-$, red: $DCOO^-$, dots: data reproduced from Figure 4A, line: fit), **C:** stopped-flow data (dots: data from Figure 5, lines: fit), **D:** PFE measurement of the rate of $HCOO^-$ oxidation at pH 6, dots: data, line: fit. Fits to the data were calculated using Eq. 1 and 2 with: $K_d^{pH\ 7\text{-}7.5}$ = 0.83 mM, $K_d^{pH\ 6}$ = 0.29 mM, k_r = 2480 s^{-1}, k_{-r} = 8060 s^{-1}, k_3 = 3930 s^{-1}, K_I = 2.00 µM, *KIE* = 4.7, k_{ox}^{PFE} = 2.0x10^5 s^{-1}, k_{red}^{PFE} = 7x10^{-4} s^{-1}, k_{PCET}^{PFE} = 1.9x10^5 s^{-1}, k_{-PCET}^{PFE} = 1.7x10^{-3} s^{-1}, k_{ox}^{sol} = 693 s^{-1}, k_{red}^{sol} = 0 s^{-1}, k_{PCET}^{sol} = 683 s^{-1}, k_{-PCET}^{sol} = 0 s^{-1}.

Figure 6 shows a representative fit to the data. The model reproduces the similar V_{max} values observed for $DCOO^-$ and $HCOO^-$ in solution assays (Figure 6A) and the very different V_{max} values observed in PFE experiments (Figure 6B), which reflect the KIE revealed by the stopped-flow experiment that is focussed most closely on C–H bond cleavage (Figure 6C). The model also reflects the KIEs observed at low formate concentrations in the solution kinetics and PFE experiments. Therefore, our model shows clearly how simple electron transfer kinetics, independent of the reaction of interest, can place the reaction in different kinetic regimes that differ significantly in the level and quality of information that they reveal. However, as may be anticipated for a simple, common model and parameter set applied to three very different experimental data sets, there are some limitations - the most substantial of which is that V_{max}^D for the solution assay data is underestimated. It is possible that the fit is compromised by the lack of a mechanism for substrate inhibition, which renders the model unable to

capture the observed decrease in $HCOO^-$ oxidation rate at high concentrations in the solution kinetics. However, it may also result from the simplicity of the formate binding mechanism applied: as discussed above, an isotope-dependent substrate binding step raises the possibility that the product of binding is not a simple Michaelis enzyme-substrate complex in which the active-site-bound formate remains unreacted, but a 'charge-transfer' intermediate in which the C–H bond is weakened. In the five-membered ring intermediate suggested in Scheme 1, the formate α-H is interacting with the sulfido ligand and electron density has shifted towards the Mo ion in either a PCET reaction (anticlockwise), or a hydride transfer reaction (clockwise).[28] Our current model does not account for an isotope sensitive formate binding rate constant.

Interpreting the steady-state data

Using the fit parameters outlined in Figure 6, the steady-state population of each catalytic intermediate can be calculated for both the solution and PFE conditions (see Supplementary Information Section 4). Figure 7 depicts the population of each species as a circle area at three $DCOO^-$ and $HCOO^-$ concentrations: below K_d (Figure 7A,D), equal to K_d (Figure 7B,E) and above K_d (Figure 7C,F).

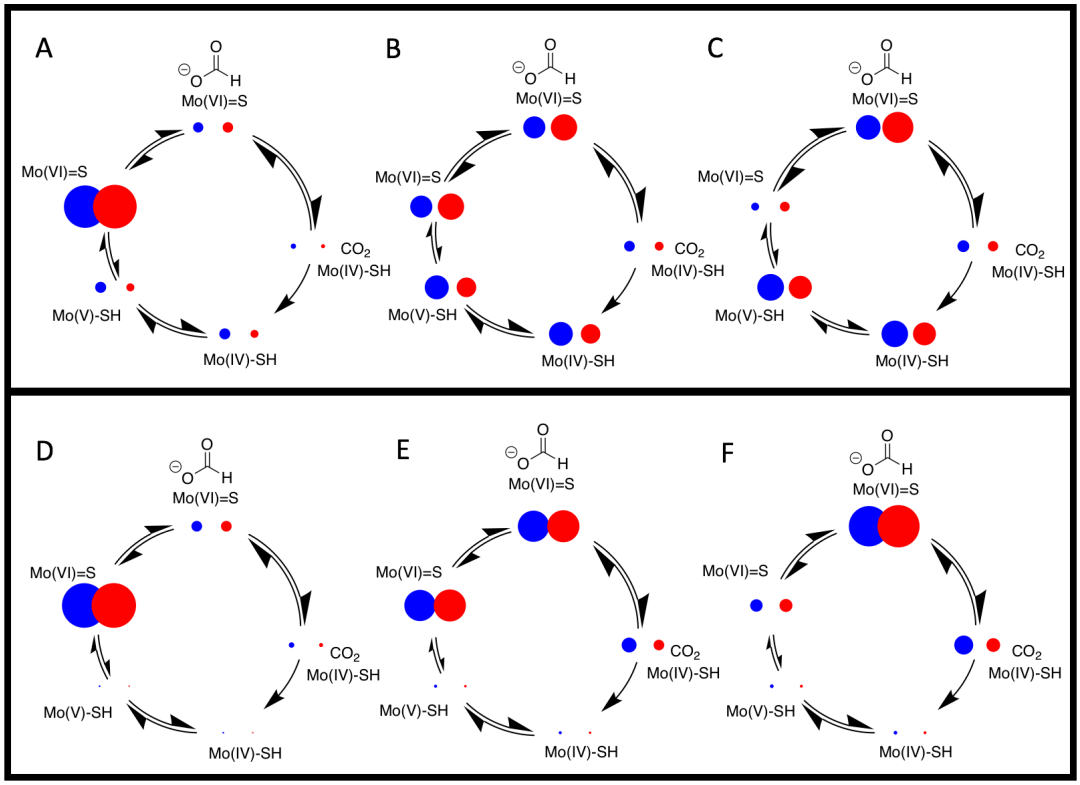

Figure 7. Steady state populations of states calculated using Eq. S16 to Eq. S19 and the parameters used to determine the fit in Figure 6. Circle areas reflect the steady-state population of each state. **A:** Simulations of solution kinetic assays with 40 μM formate, **B:** Simulations of solution kinetic assays with 0.83 mM formate, **C:** Simulations of solution kinetic assays with 10 mM formate, **D**: PFE simulations with 40 μM formate, **E**: PFE simulations with 0.83 mM formate, **F**: PFE simulations with 10 mM formate. $HCOO^-$: blue, $DCOO^-$: red.

First, the effects of the different electron transfer rates between the solution assays (slow) and PFE (fast) are clearly evident, especially at high concentrations, from the larger populations of the reduced Mo(V)–SH and Mo(IV)–SH states in the solution assay simulations (Figure 7A-C, top) than the PFE simulations (Figure 7D-F, bottom). Faster electron transfer rates shift the FDH population towards the oxidized states, making isotope-dependent steps more strongly rate determining and the KIE more pronounced.

At formate concentrations much lower than K_d (e.g. Figure 7A, D - left), the population lies towards the Mo(VI)=S state, as expected for a binding equilibrium. The populations in both the PFE and solution assay simulations appear similar in this case. The active site can be regenerated rapidly and the isotope- and formate

concentration-dependent conversion reaction (binding through to CO_2 release) controls the overall rate of catalysis. As a result, a KIE is apparent at low formate concentrations. Upon increasing the concentration of formate to equal K_d (Figure 7B, E - middle), the configurations diverge. In the fast electron transfer regime (Figure 7E, F - bottom), the population of the Mo(=S)(formate) state increases (before the isotope-dependent step), in accordance with the binding equilibrium, whilst there is a minimal increase in the populations of the reduced states. In contrast, for slow electron transfer (Figure 7B, C - top), there is a larger shift of the population into reduced states. Here, the model indicates the transfer of rate control from chemical catalysis to electron transfer and so the KIE is decreased. For the fast electron transfer regime, electron transfer still outpaces chemical catalysis and the system is held more in the Mo(=S)(formate) state. The KIE is thus larger at higher formate concentrations.

Using the predicted rate constants, it is also possible to estimate the absolute rate of formate oxidation in PFE experiments. PFE data have been normalized to account for lack of knowledge of the electroactive surface coverage. However, the behavior of FDH under high electron transfer regimes can be simulated using Eq. 1 and the best fit rate constants to give an estimated maximal rate for formate oxidation of 626 s^{-1}, around 11 times higher than in solution assays. This result underlines the importance of considering the rate of electron transfer with solution phase electron donors or acceptors when elucidating active site kinetics. Furthermore, if the rate of electron transfer in solution assays could be increased (e.g. by using an electron acceptor with a higher reduction potential) to mirror the PFE data (Figure 7F) then spectroscopic characterization of the important Mo(VI)=S($HCOO^-$)/Mo(IV)–SH(CO_2) intermediate states may become possible, especially if the solution CO_2 concentration is increased.

Evolution of species over time in the stopped flow experiment

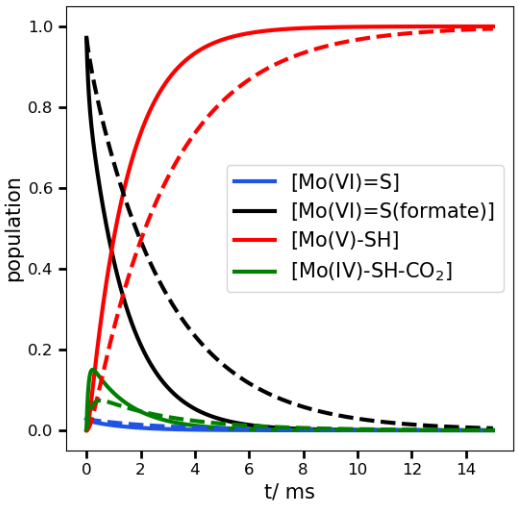

Figure 8. Calculated changes in pre-equilibrium populations of the Mo(VI)=S, Mo(VI)=S(N_3^-), Mo(VI)=S($HCOO^-$), Mo(IV)–SH(CO_2) and Mo(V)–SH states over time using equations S41-S42 and Equation 2 and the same parameters as in Figure 6 with [$HCOO^-$] = 10 mM, [N_3^-] = 0 mM. Solid lines: $HCOO^-$, dashed lines: $DCOO^-$.

The time-evolution of the four FDH states detailed for stopped-flow experiments in Scheme 1 can be simulated using the best fit parameters detailed in Figure 6, Equation 2 and equations S41 and S42. Figure 8 shows the simulation for FDH reacting with 10 mM formate in the absence of N_3^-. Due to the fast formate binding equilibrium, a steady-state ratio of Mo(VI)=S(formate) and Mo(VI)=S is established immediately, weighted towards the Mo(VI)=S(formate) state and governed by K_d. As the reaction progresses, the Mo(IV)–SH(CO_2) population grows to around 15% at about 0.2 ms. For $DCOO^-$ oxidation, the buildup is lower (7.5%) and peaks at around 0.5 ms. Such a small buildup and lifetime of this species leads to the apparent first-order behavior of the reaction (rather than biphasic behavior in which formation of the Mo(V)–SH state would exhibit a lag phase). Thus, Mo(VI)=S(formate) is rapidly converted to the product Mo(V)–SH and formate oxidation (C–H bond cleavage) exerts strong control over the net reaction rate. As a result, the KIE revealed by the stopped-flow data is considered to represent closely the intrinsic KIE for formate oxidation.

These calculations further highlight the importance of steady-state measurements in observing FDH activity. If the key Mo(VI)=S(formate)/Mo(IV)–SH(CO_2) intermediate states could be spectroscopically characterized, transient measurements would only allow a small window of time for their detection. Bringing the system into steady state, either in solution assays, or on an electrode surface, would provide a continuous observation period. The spectroscopic characterization of electroactive proteins and enzymes on electrode surfaces via techniques such as surface Raman or attenuated total reflection- infra red spectroscopies are in current use and development.[46] The control over the distribution of FDH states enabled by the electrode potential, and the ability to dynamically change conditions (such as varying formate concentration by titration as reported here) should allow the population of key intermediates to be promoted, increasing the ease with which they may be spectroscopically characterized by these techniques.

Conclusions

Our unifying model for FDH catalysis shows how the distinct kinetic behaviors of the solution assay kinetics, PFE and stopped-flow methods can be rationalized by considering the rates of chemical catalysis and intermolecular/interfacial electron transfer, and provides predictions to guide future experimental designs.

In solution assays, electron transfer between FDH and BV^{2+} is slow and a KIE of 2.77 is only apparent at low formate concentration (< 40 μM) when chemical catalysis is also slow. At higher formate concentrations (> 40 μM) and accelerated chemical catalysis, the reaction rate is limited by isotope-insensitive electron transfer. The PFE technique lifts this rate limitation through fast interfacial electron transfer between FDH and the electrode. As a result, catalysis is again limited by the chemical conversion and a KIE of 2.44 is observed. Stopped-flow kinetics enable the rate of chemical catalysis at the active site to be observed independently of intermolecular/ interfacial electron transfer and reveal a KIE for formate oxidation of approximately 3, similar to that observed at low concentration and determined by PFE. Our observation that, under experimental conditions that focus on formate oxidation itself, catalysis is both formate concentration and isotope sensitive and can be modelled by tightly coupling the formate binding and conversion steps, may suggest the possibility that the C–H bond is weakened in the initial formate-bound state, better represented as a bound intermediate, between CO_2 and formate. Finally, by extrapolating our model to as-yet unexplored experimental conditions, we highlight the regimes of formate concentration and electron transfer under which the concentrations of key substrate/product-bound FDH states, including the proposed intermediate, may be enhanced to allow them to be observed spectroscopically. The presented model of FDH catalysis of formate oxidation could be easily transposed into a model for CO_2 reduction (or catalysis in both directions). Therefore, this framework will provide a starting point in rationalizing similar data for CO_2 reduction. Furthermore, since formate oxidation and CO_2 reduction are inextricably linked in a mechanistic sense, we expect our observations on formate oxidation to reflect on data for CO_2 reduction. A particularly crucial aspect is elucidating the structure and behavior of the intermediate which is likely formed during the catalytic interconversion step.

Acknowledgements

This research was supported by BBSRC (BB/I026367/1 and BB/J000124/1), EPSRC NanoDTC Cambridge (EP/L015978/1), The Medical Research Council (MC_U105663141) and an ERC Consolidator Grant 'MatEnSAP' (682833).

Supporting Information

Supporting data, further details on the mathematical model, equations and parameters, and a description of the fitting algorithm are given in the Supporting Information.
Raw data related to this publication are available at the University of Cambridge data repository: https://doi.org/XXX [link to be completed upon acceptance]

References

(1) Reda, T.; Plugge, C. M.; Abram, N. J.; Hirst, J. Reversible Interconversion of Carbon Dioxide and Formate by an Electroactive Enzyme. *Proc. Natl. Acad. Sci. U. S. A.* **2008**, *105*, 10654–10658.

(2) Bassegoda, A.; Madden, C.; Wakerley, D. W.; Reisner, E.; Hirst, J. Reversible Interconversion of CO_2 and Formate by a Molybdenum-Containing Formate Dehydrogenase. *J. Am. Chem. Soc.* **2014**, *136*, 15473–15476.

(3) Nielsen, C. F.; Lange, L.; Meyer, A. S. Classification and Enzyme Kinetics of Formate Dehydrogenases for Biomanufacturing via CO_2 Utilization. *Biotechnol. Adv.* **2019**, *37*, 107408.

(4) Maia, L. B.; Fonseca, L.; Moura, I.; Moura, J. J. G. Reduction of Carbon Dioxide by a Molybdenum-Containing Formate Dehydrogenase: A Kinetic and Mechanistic Study. *J. Am. Chem. Soc.* **2016**, *138*, 8834–8846.

(5) Hartmann, T.; Leimkühler, S. The Oxygen-Tolerant and NAD^+ -Dependent Formate Dehydrogenase from *Rhodobacter Capsulatus* Is Able to Catalyze the Reduction of CO_2 to Formate. *FEBS J.* **2013**, *280*, 6083–6096.

(6) Yu, X.; Niks, D.; Mulchandani, A.; Hille, R. Efficient Reduction of CO_2 by the Molybdenum-Containing Formate Dehydrogenase from *Cupriavidus Necator* (*Ralstonia Eutropha*). *J. Biol. Chem.* **2017**, *292*, 16872–16879.

(7) Graentzdoerffer, A.; Rauh, D.; Pich, A.; Andreesen, J. R. Molecular and Biochemical Characterization of Two Tungsten- and Selenium-Containing Formate Dehydrogenases from *Eubacterium Acidaminophilum* That Are Associated with Components of an Iron-Only Hydrogenase. *Arch. Microbiol.* **2003**, *179*, 116–130.

(8) Schuchmann, K.; Müller, V. Direct and Reversible Hydrogenation of CO_2 to Formate by a Bacterial Carbon Dioxide Reductase. *Science* **2013**, *342*, 1382–1385.

(9) Sakai, K.; Kitazumi, Y.; Shirai, O.; Kano, K. Bioelectrocatalytic Formate Oxidation and Carbon Dioxide Reduction at High Current Density and Low Overpotential with Tungsten-Containing Formate Dehydrogenase and Mediators. *Electrochem. commun.* **2016**, *65*, 31–34.

(10) Min, K.; Park, Y.-S.; Park, G. W.; Lee, J.; Moon, M.; Ko, C. H.; Lee, J.-S. Elevated Conversion of CO_2 to Versatile Formate by a Newly Discovered Formate Dehydrogenase from *Rhodobacter Aestuarii*. *Bioresour. Technol.* **2020**, *305*, 123155.

(11) Milton, R. D.; Ruth, J. C.; Deutzmann, J. S.; Spormann, A. M. *Methanococcus Maripaludis* Employs Three Functional Heterodisulfide Reductase Complexes for Flavin-Based Electron Bifurcation Using Hydrogen and Formate. *Biochemistry* **2018**, *57*, 4848–4857.

(12) Sokol, K. P.; Robinson, W. E.; Oliveira, A. R.; Warnan, J.; Nowaczyk, M. M.; Ruff, A.; Pereira, I. A. C.; Reisner, E. Photoreduction of CO_2 with a Formate Dehydrogenase Driven by Photosystem II Using a Semi-Artificial Z-Scheme Architecture. *J. Am. Chem. Soc.* **2018**, *140*, 16418–16422.

(13) Miller, M.; Robinson, W. E.; Oliveira, A. R.; Heidary, N.; Kornienko, N.; Warnan, J.; Pereira, I. A. C.; Reisner, E. Interfacing Formate Dehydrogenase with Metal Oxides for the Reversible Electrocatalysis and Solar-Driven Reduction of Carbon Dioxide. *Angew. Chemie Int. Ed.* **2019**, *58*, 4601–4605.

(14) Kuk, S. K.; Gopinath, K.; Singh, R. K.; Kim, T.-D.; Lee, Y.; Choi, W. S.; Lee, J.-K.; Park, C. B. NADH-Free Electroenzymatic Reduction of CO_2 by Conductive Hydrogel-Conjugated Formate Dehydrogenase. *ACS Catal.* **2019**, *9*, 5584–5589.

(15) Noji, T.; Jin, T.; Nango, M.; Kamiya, N.; Amao, Y. CO_2 Photoreduction by Formate Dehydrogenase and a Ru-Complex in a Nanoporous Glass Reactor. *ACS Appl. Mater. Interfaces* **2017**, *9*, 3260–3265.

(16) Parkinson, B. A.; Weaver, P. F. Photoelectrochemical Pumping of Enzymatic CO_2 Reduction. *Nature* **1984**, *309*, 148–149.

(17) Sahin, S.; Cai, R.; Milton, R. D.; Abdellaoui, S.; Macazo, F. C.; Minteer, S. D. Molybdenum-Dependent Formate Dehydrogenase for Formate Bioelectrocatalysis in a Formate/O_2 Enzymatic Fuel Cell. *J. Electrochem. Soc.* **2018**, *165*, H109–H113.

(18) Sokol, K. P.; Robinson, W. E.; Oliveira, A. R.; Zacarias, S.; Lee, C.-Y.; Madden, C.; Bassegoda, A.; Hirst, J.; Pereira, I. A. C.; Reisner, E. Reversible and Selective Interconversion of Hydrogen and Carbon Dioxide into Formate by a Semiartificial Formate Hydrogenlyase Mimic. *J. Am. Chem. Soc.* **2019**, *141*, 17498–17502.

(19) Niks, D.; Hille, R. Molybdenum- and Tungsten-Containing Formate Dehydrogenases and Formylmethanofuran Dehydrogenases: Structure, Mechanism, and Cofactor Insertion. *Protein Sci.* **2019**, *28*, 111–122.

(20) Jormakka, M.; Törnroth, J.; Byrne, B.; Iwata, S. Molecular Basis of Proton Motive Force Generation: Structure of Formate Dehydrogenase-N. *Science* **2002**, *295*, 1863–1868.

(21) Boyington, J. C.; Gladyshev, V. N.; Khangulov, S. V.; Stadtman, T. C.; Sun, P. D. Crystal Structure of Formate Dehydrogenase H: Catalysis Involving Mo, Molybdopterin, Selenocysteine, and an Fe_4S_4 Cluster. *Science* **1997**, *275*, 1305–1308.

(22) Raaijmakers, H.; Macieira, S.; Dias, J. M.; Teixeira, S.; Bursakov, S.; Huber, R.; Moura, J. J. G.; Moura, I.; Romão, M. J. Gene Sequence and the 1.8 Å Crystal Structure of the Tungsten-Containing Formate Dehydrogenase from *Desulfovibrio Gigas*. *Structure* **2002**, *10*, 1261–1272.

(23) Wagner, T.; Ermler, U.; Shima, S. The Methanogenic CO_2 Reducing-and-Fixing Enzyme Is Bifunctional and Contains 46 [4Fe-4S] Clusters. *Science* **2016**, *354*, 114–117.

(24) Oliveira, A. R.; Mota, C.; Mourato, C.; Domingos, R. M.; Santos, M. F. A.; Gesto, D.; Guigliarelli, B.; Santos-Silva, T.; Romão, M. J.; Cardoso Pereira, I. A. Toward the Mechanistic Understanding of Enzymatic CO_2 Reduction. *ACS Catal.* **2020**, *10*, 3844–3856.

(25) Thomé, R.; Gust, A.; Toci, R.; Mendel, R.; Bittner, F.; Magalon, A.; Walburger, A. A Sulfurtransferase Is Essential for Activity of Formate Dehydrogenases in *Escherichia Coli*. *J. Biol. Chem.* **2012**, *287*, 4671–4678.

(26) Schrapers, P.; Hartmann, T.; Kositzki, R.; Dau, H.; Reschke, S.; Schulzke, C.; Leimkühler, S.; Haumann, M. Sulfido and Cysteine Ligation Changes at the Molybdenum Cofactor during Substrate Conversion by Formate Dehydrogenase (FDH) from *Rhodobacter Capsulatus*. *Inorg. Chem.* **2015**, *54*, 3260–3271.

(27) Khangulov, S. V.; Gladyshev, V. N.; Dismukes, G. C.; Stadtman, T. C. Selenium-Containing Formate Dehydrogenase H from *Escherichia Coli* : A Molybdopterin Enzyme That Catalyzes Formate Oxidation without Oxygen Transfer. *Biochemistry* **1998**, *37*, 3518–3528.

(28) Robinson, W. E.; Bassegoda, A.; Reisner, E.; Hirst, J. Oxidation-State-Dependent Binding Properties of the Active Site in a Mo-Containing Formate Dehydrogenase. *J. Am. Chem. Soc.* **2017**, *139*, 9927–9936.

(29) Axley, M. J.; Böck, A.; Stadtman, T. C. Catalytic Properties of an *Escherichia Coli* Formate Dehydrogenase Mutant in Which Sulfur Replaces Selenium. *Proc. Natl. Acad. Sci. U. S. A.* **1991**, *88*, 8450–8454.

(30) Duffus, B. R.; Schrapers, P.; Schuth, N.; Mebs, S.; Dau, H.; Leimkühler, S.; Haumann, M. Anion Binding and Oxidative Modification at the Molybdenum Cofactor of Formate Dehydrogenase from Rhodobacter Capsulatus Studied by X-Ray Absorption Spectroscopy. *Inorg. Chem.* **2020**, *59*, 214–225.

(31) Cordas, C. M.; Moura, J. J. G. Molybdenum and Tungsten Enzymes Redox Properties – A Brief Overview. *Coord. Chem. Rev.* **2019**, *394*, 53–64.

(32) Walker, L. M.; Li, B.; Niks, D.; Hille, R.; Elliott, S. J. Deconvolution of Reduction Potentials of Formate Dehydrogenase from Cupriavidus Necator. *J. Biol. Inorg. Chem.* **2019**, *24*, 889–898.

(33) Gladyshev, V. N.; Khangulov, S. V; Axley, M. J.; Stadtman, T. C. Coordination of Selenium to Molybdenum in Formate Dehydrogenase H from *Escherichia Coli*. *Proc. Natl. Acad. Sci. U. S. A.* **1994**, *91*, 7708–7711.

(34) Rivas, M. G.; González, P. J.; Brondino, C. D.; Moura, J. J. G.; Moura, I. EPR Characterization of the Molybdenum(V) Forms of Formate Dehydrogenase from *Desulfovibrio Desulfuricans* ATCC 27774 upon Formate Reduction. *J. Inorg. Biochem.* **2007**, *101*, 1617–1622.

(35) Niks, D.; Duvvuru, J.; Escalona, M.; Hille, R. Spectroscopic and Kinetic Properties of the Molybdenum-Containing, NAD^+ -Dependent Formate Dehydrogenase from *Ralstonia Eutropha*. *J. Biol. Chem.* **2016**, *291*, 1162–1174.

(36) Helm, M. L.; Stewart, M. P.; Bullock, R. M.; DuBois, M. R.; DuBois, D. L. A Synthetic Nickel Electrocatalyst with a Turnover Frequency Above 100,000 s^{-1} for H_2 Production. *Science* **2011**, *333*, 863–866.

(37) Le Goff, A.; Artero, V.; Jousselme, B.; Tran, P. D.; Guillet, N.; Metaye, R.; Fihri, A.; Palacin, S.; Fontecave, M. From Hydrogenases to Noble Metal-Free Catalytic Nanomaterials for H_2 Production and Uptake. *Science* **2009**, *326*, 1384–1387.

(38) Laureanti, J. A.; Ginovska, B.; Buchko, G. W.; Schenter, G. K.; Hebert, M.; Zadvornyy, O. A.; Peters, J. W.; Shaw, W. J. A Positive Charge in the Outer Coordination Sphere of an Artificial Enzyme Increases CO_2 Hydrogenation. *Organometallics* **2020**, *39*, 1532–1544.

(39) Cunningham, D. W.; Barlow, J. M.; Velazquez, R. S.; Yang, J. Y. Reversible and Selective CO_2 to HCO_2^- Electrocatalysis near the Thermodynamic Potential. *Angew. Chemie Int. Ed.* **2020**, *59*, 4443–4447.

(40) Fourmond, V.; Wiedner, E. S.; Shaw, W. J.; Léger, C. Understanding and Design of Bidirectional and Reversible Catalysts of Multielectron, Multistep Reactions. *J. Am. Chem. Soc.* **2019**, *141*, 11269–11285.

(41) Fourmond, V.; Lautier, T.; Baffert, C.; Leroux, F.; Liebgott, P.-P.; Dementin, S.; Rousset, M.; Arnoux, P.; Pignol, D.; Meynial-Salles, I.; Soucaille, P.; Bertrand, P.; Léger, C. Correcting for Electrocatalyst Desorption and Inactivation in Chronoamperometry Experiments. *Anal. Chem.* **2009**, *81*, 2962–2968.

(42) Axley, M. J.; Grahame, D. A. Kinetics for Formate Dehydrogenase of Escherichia Coli Formate-Hydrogenlyase. *J. Biol. Chem.* **1991**, *266*, 13731–13736.

(43) Léger, C.; Bertrand, P. Direct Electrochemistry of Redox Enzymes as a Tool for Mechanistic Studies. *Chem. Rev.* **2008**, *108*, 2379–2438.

(44) Moser, C. C.; Farid, T. A.; Chobot, S. E.; Dutton, P. L. Electron Tunneling Chains of Mitochondria. *Biochim. Biophys. Acta - Bioenerg.* **2006**, *1757*, 1096–1109.

(45) Raaijmakers, H. C.; Romão, M. J. Formate-Reduced *E. Coli* Formate Dehydrogenase H: The Reinterpretation of the Crystal Structure Suggests a New Reaction Mechanism. *J. Biol. Inorg. Chem.* **2006**, *11*, 849–854.

(46) Kornienko, N.; Ly, K. H.; Robinson, W. E.; Heidary, N.; Zhang, J. Z.; Reisner, E. Advancing Techniques for Investigating the Enzyme–Electrode Interface. *Acc. Chem. Res.* **2019**, *52*, 1439–1448.

ToC artwork

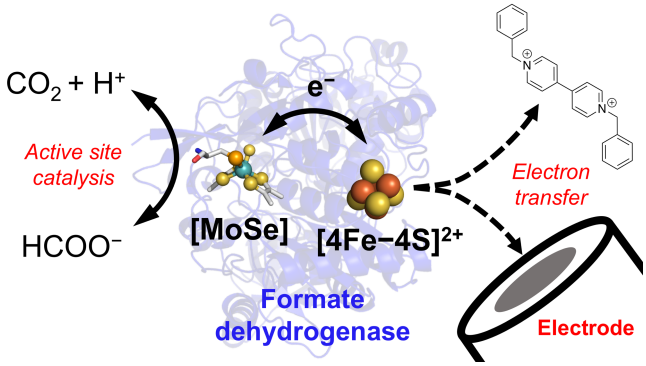
$CO_2 + H^+$
Active site catalysis
$HCOO^-$
e^-
[MoSe]
$[4Fe{-}4S]^{2+}$
Formate dehydrogenase
Electron transfer
Electrode